

High area-capacity Mg batteries enabled by sulfur/copper integrated cathode design

Zhenfang Zhou^{a,1}, Aobing Du^{b,1}, Weijie Kong^a, Zhuang Chen^a, Zhonghua Zhang^{a,b,*}, Bingbing Chen^c, Yitao He^d, Shanmu Dong^b, Zhenjiang Li^a, Guicun Li^{a,*}, Guanglei Cui^{b,*}

^a College of Materials Science and Engineering, Qingdao University of Science and Technology, Qingdao 266042, Shandong, China

^b Qingdao Industrial Energy Storage Research Institute, Qingdao Institute of Bioenergy and Bioprocess Technology, Chinese Academy of Sciences, Qingdao 266101, Shandong, China

^c Department of Energy Science and Engineering, Nanjing Tech University, Nanjing 211816, Jiangsu, China

^d Department of Physics, Harbin Institute of Technology, Harbin 150001, Heilongjiang, China

¹These authors contributed equally to this work.

*Corresponding authors.

E-mail addresses: zhangzh@qust.edu.cn (Z. Zhang), guicunli@qust.edu.cn (G. Li), cuigl@qibebt.ac.cn (G. Cui).

This profile contains experimental section, Fig. S1 to Fig. S23 and Table S1.

Experimental Section

Synthetic procedures: The sulfur/copper-foil integrated cathodes (abbreviated as the S@Cu foil electrode) are fabricated by the typical blade-coating method. Specifically, the slurry containing sublimed sulfur, PVDF binders and carbon black with weight ratio of 7:1:2 is blade-coated on copper foil. For comparison, pure sulfur/aluminum cathodes are also fabricated via blade-coating the slurry on an aluminum foil (abbreviated as the S@Al electrode). The sulfur loading in each electrode is controlled to be around 3.0 mg cm⁻².

To construct an ultrahigh areal capacity Mg battery, a three-dimensional Cu foam and a facile slurry-dipping method are utilized (the slurry contains sublimed sulfur, PVDF binder, and carbon black with weight ratio of 7:1:2) to fabricate the sulfur/copper-foam integrated cathode (abbreviated as S@Cu foam electrode). Firstly, Cu foam (Changsha Lyrin Material Co., Ltd.) of approximately 1.0 mm thickness was cut into rectangle (70 mm × 35 mm) and immersed into 1.0 M HCl solution for 10 min to remove the oxides on the surface. It was then washed with DI water and ethanol for several

times, and dried under vacuum at room temperature for further using. Controlling the dipping times can easily fabricate the S@Cu foam electrode (1.2 cm^2) with varied sulfur mass loading ranging from 12.5 mg cm^{-2} to 33.3 mg cm^{-2} . Specifically, the cleaned Cu foam is immersed into the slurry for 2 mins, which is then dried at $60\text{ }^{\circ}\text{C}$ to achieve the S@Cu foam electrode with sulfur mass loading of about 10 mg cm^{-2} . It should be noted that both the concentration and viscosity of the slurry play a role in determining the sulfur mass loading. To achieve higher mass loading electrodes, the S@Cu foam electrode is repeatedly immersed into the slurry for several minutes.

Cell fabrication and electrochemical measurements: The 2032-type coin cells are assembled to evaluate the electrochemical performances of varied cathodes as fabricated above. The polished Mg foil with a diameter of around 1.0 cm is utilized as anode. The 0.5 M OMBB electrolyte is served as Mg-ion electrolyte and the glass microfiber filter is used as separator between cathode and anode.

The CV curves are tested on a Biologic VMP-300 potentiostat at a scan rate of 0.02 mV s^{-1} . The galvanostatic discharge/charge experiments are conducted on a LAND CT2001A system within a voltage range from 0.4 V to 2.0 V vs. Mg^{2+}/Mg . It should be noted that the galvanostatic discharge/charge experiments are conducted at different temperatures ($50\text{ }^{\circ}\text{C}$ or $25\text{ }^{\circ}\text{C}$). The applied current density varies from the tested cathodes accordingly. For the cycle performances, the S@Cu foil electrode is galvanostatically charged and discharged at 0.5 mA cm^{-2} and at $50\text{ }^{\circ}\text{C}$. The S@Cu foam electrode is also galvanostatically charged and discharged at 0.1 mA cm^{-2} and at $50\text{ }^{\circ}\text{C}$. The EIS experiments are tested on the same potentiostat to that of the CV experiments in a frequency range from 1.0 MHz to 1.0 Hz using an amplitude voltage of 10.0 mV . As for the cycled Mg battery, an electrochemical activation process has been initially conducted in a way of repeatedly charging/discharging under a low current density of 0.1 mA g^{-1} for 3 cycles. The GITT experiment

is conducted on a LAND CT2001A system. The Mg battery is galvanostatic discharged/charged for 0.5 h at 20 mA g⁻¹ and relaxed for 0.5 h to reach a quasi-equilibrium state.

Materials characterizations: A series of *ex-situ* experiments are conducted to investigate the reaction mechanism of the S@Cu foil electrode. The cell disassembly experiments are carried out in a glovebox filled with argon and the H₂O and O₂ concentrations are controlled to be less than 0.1 ppm. The XRD experiments of the cycled electrode are conducted on a Bruker D8 diffractometer using Cu K_α radiation. The morphology of the cycled products is investigated by a field-emission SEM on Hitachi S-4800 equipment and TEM on a JEOLJEM-2010F microscope. The element distribution of the fully discharged electrode is also investigated by the energy dispersive spectrometry (EDS) conducted on the same FE-SEM equipment. The HRTEM images combined with selected area electron diffraction (SAED) patterns are also investigated on the same microscope at an acceleration voltage of 200 kV. The high-resolution TEM experiments are also conducted on a JEOL-ARM200F equipped with a Cs image corrector at 200 kV to directly visualize the atomic occupation in the discharged products of MgS crystal. The XPS experiments are also conducted to analyse the chemical environments of the discharge/charge products on a Perkin-Elmer PHI 550 spectrometer using Al K_α (1486.6 eV) as the X-ray source. The ultraviolet–visible (UV-vis) absorption spectra of copper sulfides synthesized by solid-state method and the electrolyte-soaked S@Cu foam electrode are collected on a Shimadzu UV-2600 spectrophotometer (Japan) from 200 to 1600 nm. The photoluminescence (PL) spectra are recorded using an EDINBURGH INSTRUMENTS FLS920 spectrometer.

The stripping/plating processes of Mg were carried out at room temperature using a two-electrode cell consisting of Cu foil as the working electrode and Mg foil as the counter electrode. A certain

amount of Mg ($0.5\text{--}30\text{ mAh cm}^{-2}$) was plated onto the Cu foil and then charged to 1.0 V (vs. Mg) to strip the Mg at different current densities. The S@Cu foam electrode after 6 cycles were disassembled in an Ar-filled glove box and reassembled the new CR2032 coin-type cell with a fresh Mg foil anode, a new separator and 200 μL of electrolyte.

First-principles calculations: The first-principles calculations are employed to analyse the electrochemical reaction pathways of copper sulfides with Cu defects using the Vienna Ab-initio Simulation Package code with the projector-augmented wave method based on density functional theory. In our calculation, the Perdew-Burke-Ernzerhof exchange-correlational functional methods are used. The energy cutoff of 500 eV and the Monkhorst-Pack K-point mesh of $5\times 5\times 5$ are set to calculate the electronic wavefunctions. The atomic coordinates in the copper sulfide structures are optimized until the maximum residual force is below 0.03 eV \AA^{-1} . The Mg ion migration energy barriers are also computed by the climbing image nudged elastic band method.

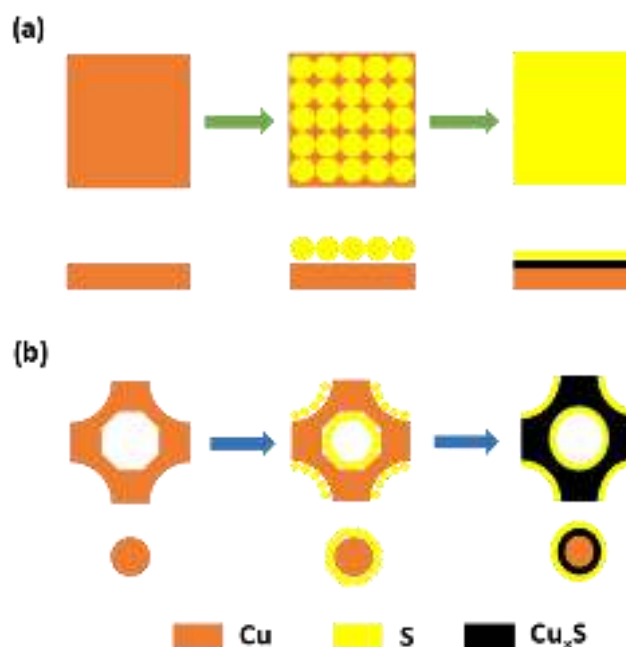


Fig. S1 Schematic illustration of the *in-situ* reaction between copper foam and sulfur at a given temperature: (a) shows the planform and the front view picture of reaction process; (b) shows the changes in cross-section view of one skeletal structure during the *in-situ* reaction.

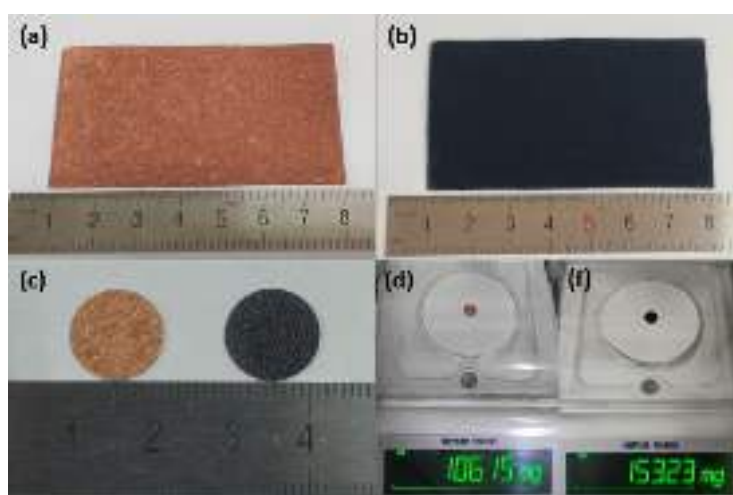


Fig. S2 Digital photographs of the pristine copper foam (a) and the S@Cu foam cathode (b); Diameter measurements (c) and weight measurement of both pristine copper foam (d) and the S@Cu foam cathode (f).

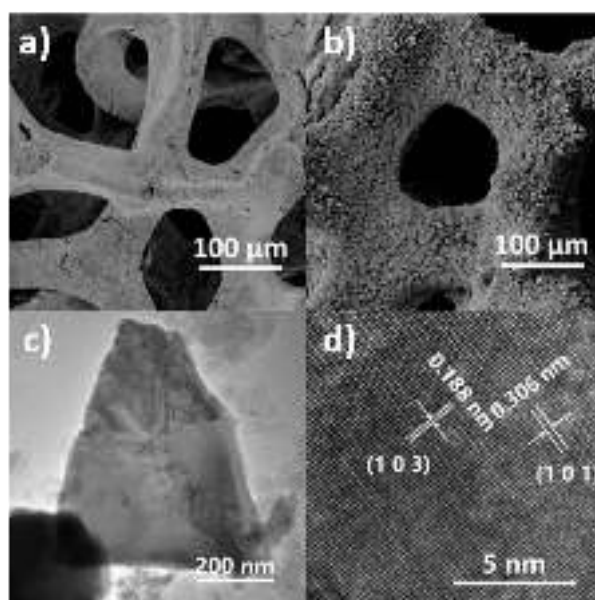


Fig. S3 SEM images of the pristine Cu foam (a) and the S@Cu foam cathodes (b); TEM image (c) and the corresponding HRTEM image (d) of the sediments on S@Cu foam cathodes.

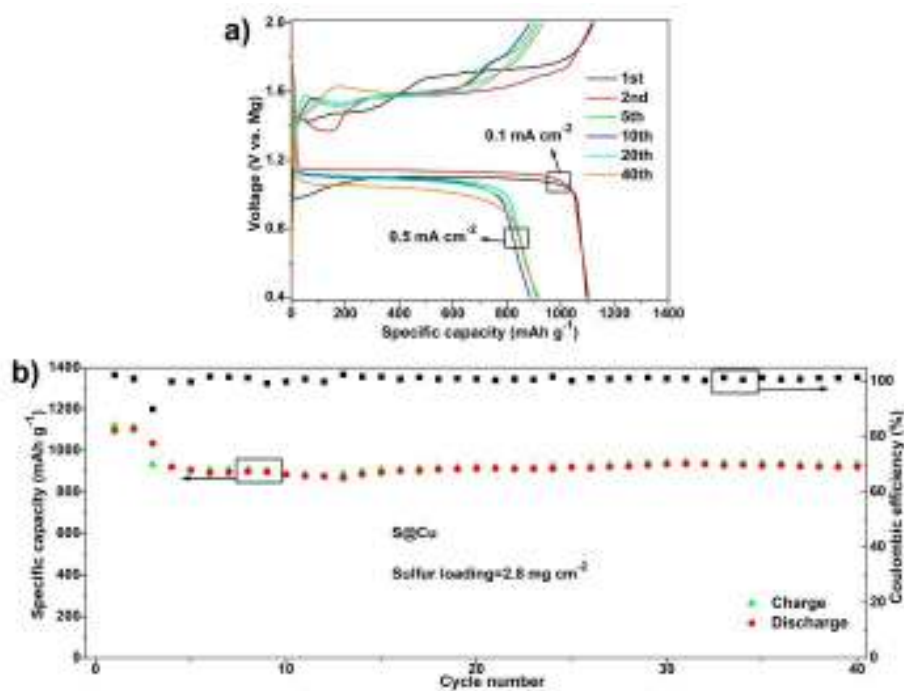


Fig. S4 Galvanostatic charge-discharge profiles (a) and cycling performance (b) of S@Cu foil electrode at 50 °C with sulfur mass loading of 2.8 mg cm⁻².

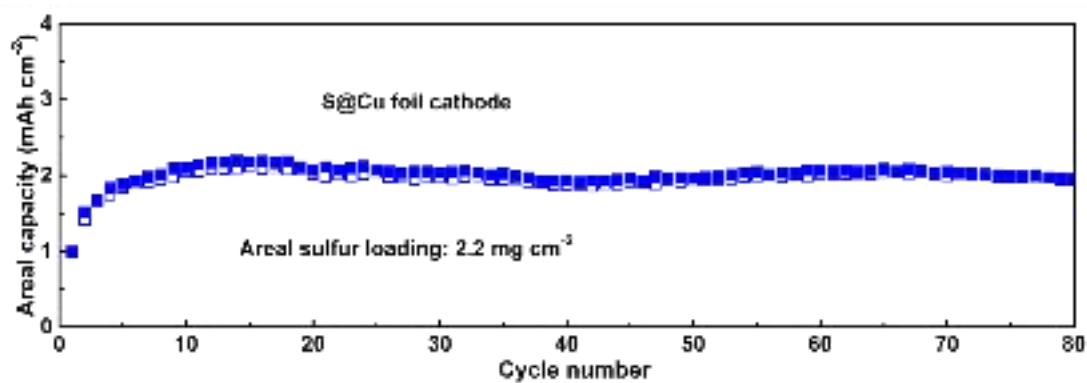


Fig. S5 The cycling performances of the S@Cu foil cathode with relatively low sulfur loading (2.2 mg cm⁻²).

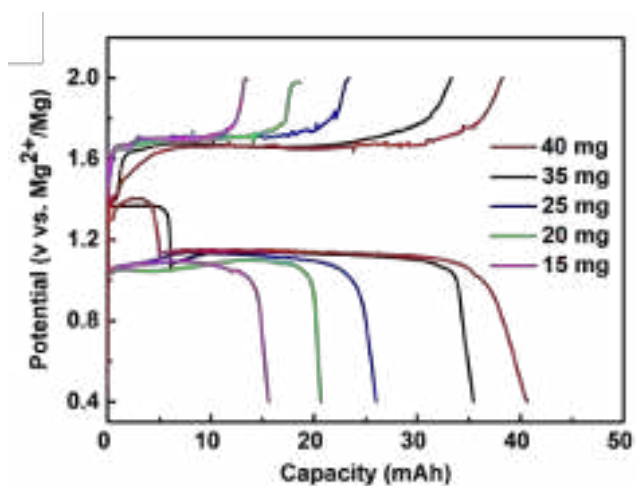


Fig. S6 The representative galvanostatic charge-discharge profiles of the S@Cu foam electrode with varied sulfur loadings.

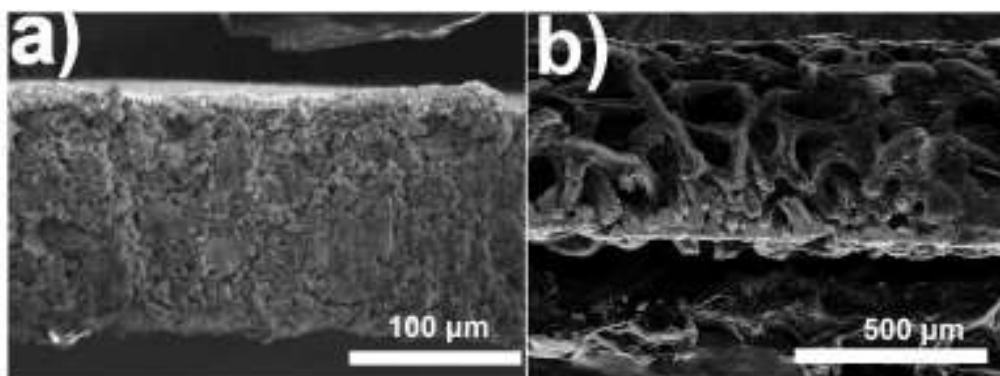


Fig. S7 Typical cross-section SEM images of the S@Cu foil electrode (a) with a sulfur loading of $\sim 3.5 \text{ mg cm}^{-2}$ and the S@Cu foam electrode (b) with a Sulfur loading of $\sim 29.2 \text{ mg cm}^{-2}$, respectively.

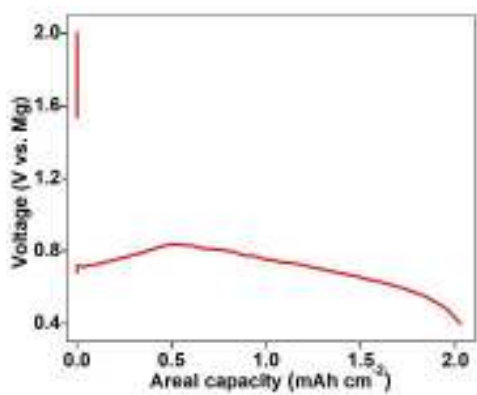


Fig. S8 The galvanostatic charge-discharge profile of the S@Ni foam electrode at a sulfur mass loading of $\sim 9.1 \text{ mg cm}^{-2}$.

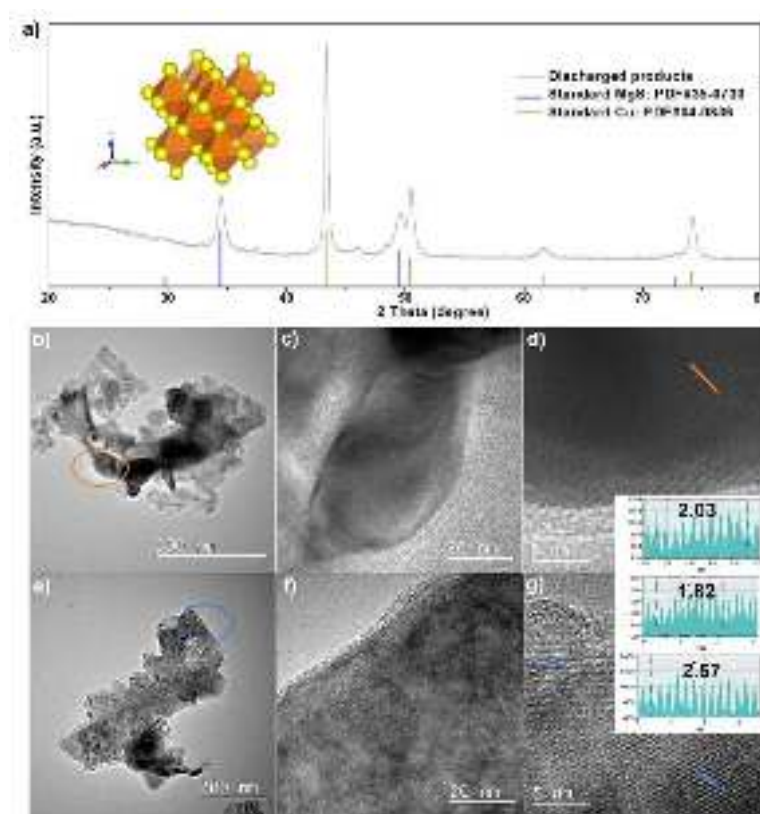


Fig. S9 Enlarged XRD pattern (a) of the discharged products. The inset shows the crystal structure of MgS; TEM images (b, c and e, f) of the discharged products; HRTEM images (d and g) of the discharged products. The insets show the interplanar interspacing of the selected regions shown in d and g.

The discharged products are observed to comprise of long-range wire-like structures (Fig. S9b) and nanoparticles (Fig. S9e). The wire-like microstructures are aggregated by small nanorods with an average width of 43 nm as shown in Fig. S9c. HRTEM image (Fig. S9d) of the nanorods demonstrates the formation of wire-like metallic copper structures. As shown in Fig. S9e and S9f, the highly porous particles are constructed by nanoparticles in a diameter range from ten to twenty nanometers. Lattice fringes of 1.82 Å and 2.57 Å are clearly observed in HRTEM image (Fig. S9g), corresponding to the (220) and (200) lattice planes of rock-salt MgS.

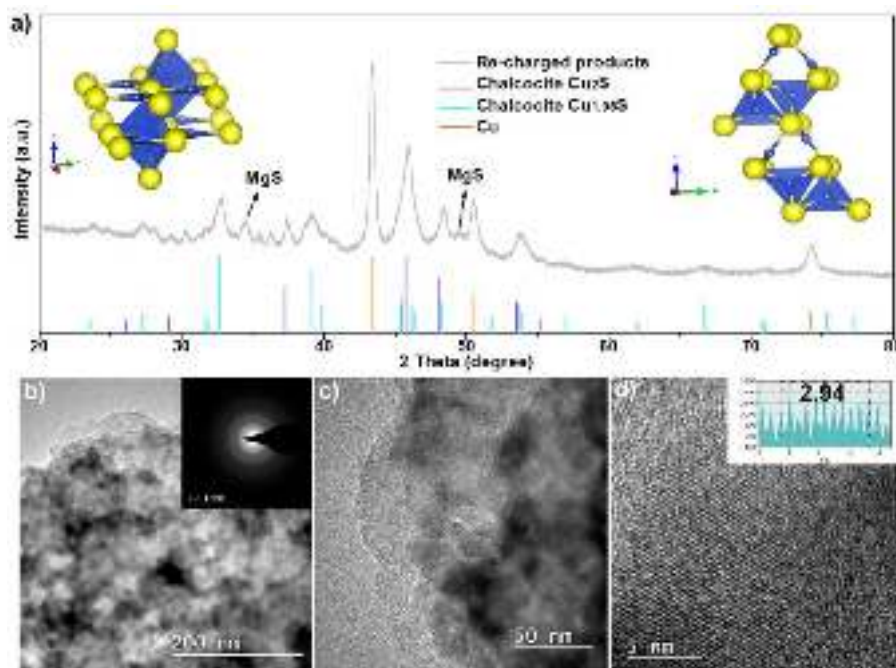


Fig. S10 XRD pattern of the recharged products. The insets show the crystal structure of two representative discharged products: Chalcocite Cu_2S and Chalcocite $\text{Cu}_{1.96}\text{S}$; TEM images (b and c) of the recharged products. The inset in (b) shows the corresponding SAED pattern; HRTEM image (d) of the recharged products. The inset show the interplanar interspacing of the selected regions shown in (d).

As shown in TEM images of Fig. S10b and S10c, the recharged products are composed of nanoparticles with low crystallinity. The SAED pattern in Fig. S10b might indicate the existence of amorphous phases. The lattice fringes of 0.30 nm in Fig. S10d correspond to the (101) lattice planes of Chalcocite Cu_2S phase.

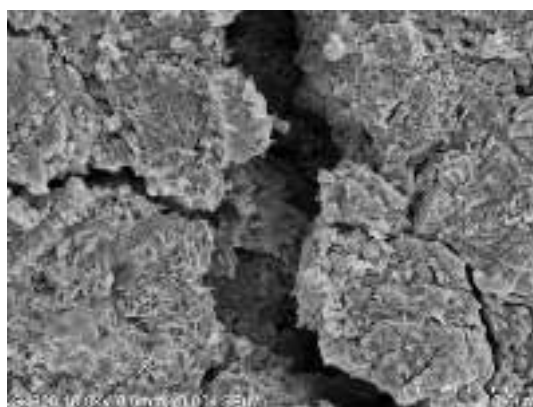


Fig. S11 SEM images of the S@Cu foil electrode at fully recharged state.

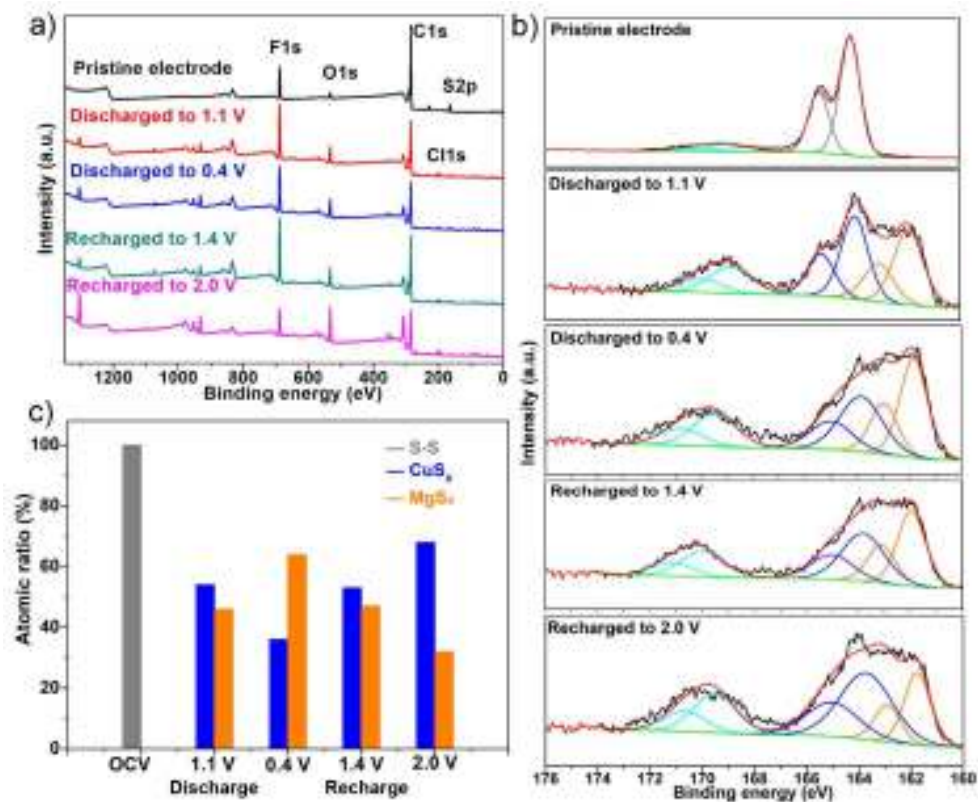


Fig. S12 XPS curve (a) of the S@Cu foil electrode at different charge-discharge states; High-resolution XPS S2p spectra (b) of the S@Cu foil electrode at different charge-discharge states; (c) displays the relative atomic ratio of Cu-S_x and/or Mg-S_x to S-S species.

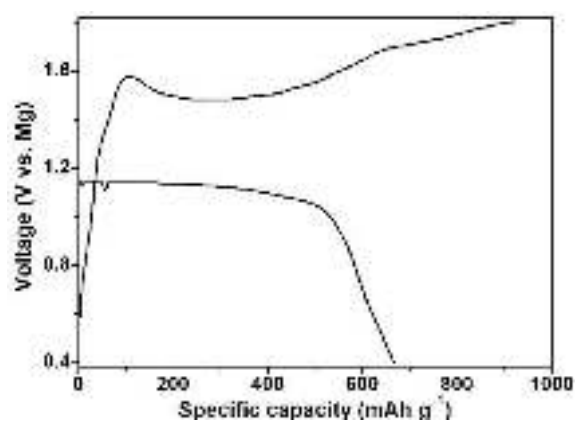


Fig. S13 Galvanostatic charge-discharge profiles of the magnesium sulfide@copper electrode at 50 °C.

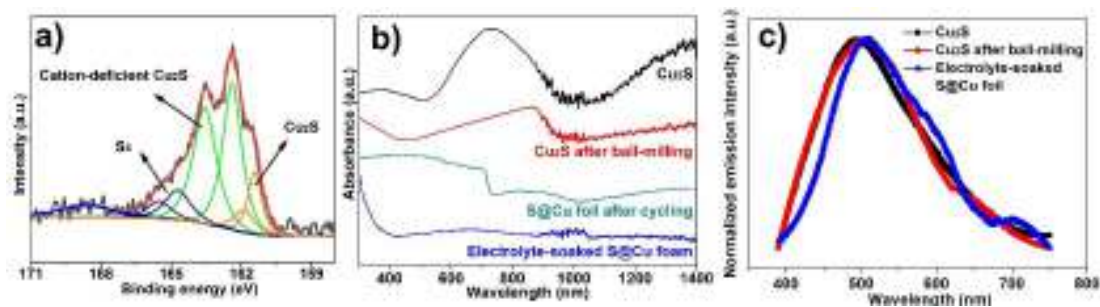


Fig. S14 (a) The S2p XPS spectra of the S@Cu foam electrode after soaking in OMBB electrolytes for 12 hrs; The UV-vis absorption (b) and PL (c) spectra of the Cu₂S synthesized by solid-state method, the ball-milling Cu₂S, the S@Cu foil electrode after cycling and the S@Cu foam electrode after soaking in OMBB electrolytes for 12 hrs.

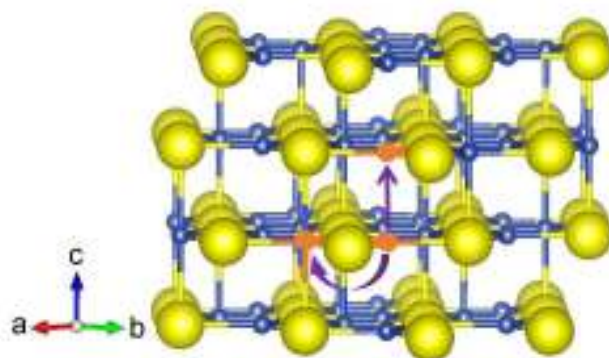


Fig. S15 Two predicted diffusion pathways of Mg ions from Cu₂ site to Cu₂ site and Cu₂ site to Cu₁ site viewed along [110] orientation.

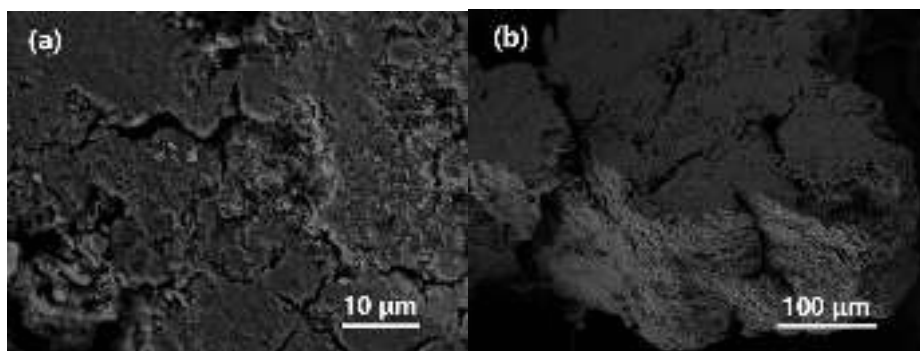


Fig. S16 SEM image (a) surface and (b) cross-sectional of the Mg anode in S@Cu foam//Mg battery configuration after 6th cycles.

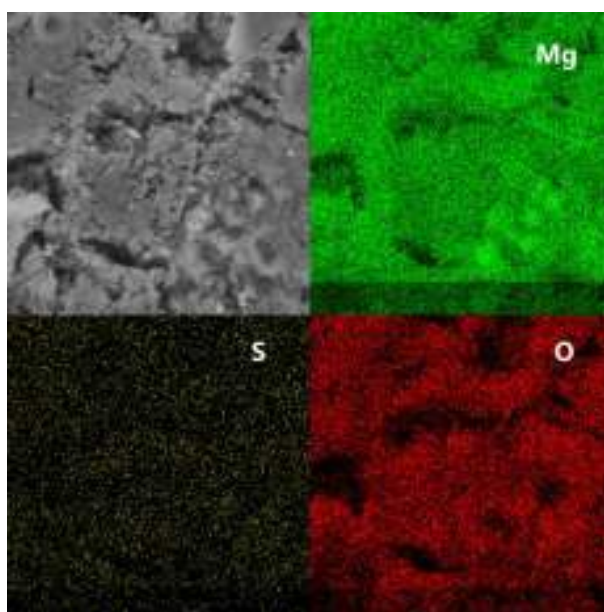


Fig. S17 EDS-mapping image of the cycled Mg anode in S@Cu foam//Mg battery configuration.

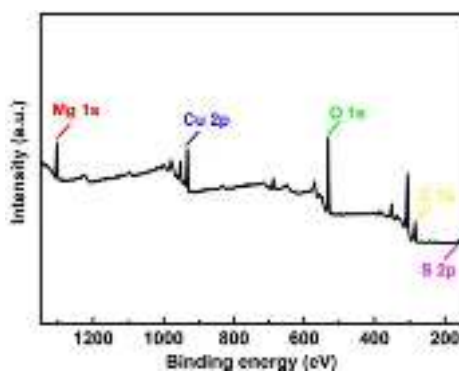


Fig. S18 XPS pattern of Mg anode in S@Cu foam//Mg battery configuration after 6th cycles.

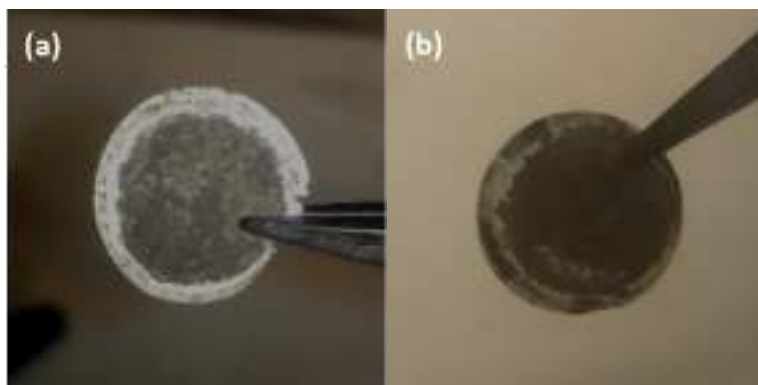


Fig. S19 Digital photographs of the sandwich separator after 1st cycle (a) and 6th cycles (b) in full cell Mg-metal battery configuration.

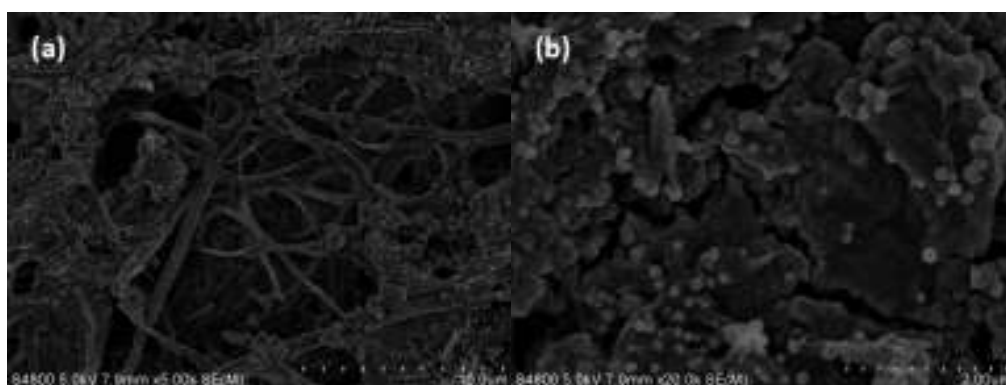


Fig. S20 SEM images of the cellulose separator in full cell Mg-metal battery configuration after 6th cycles (a). (b) is magnified images of (a).

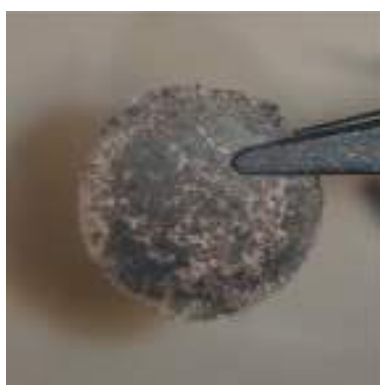


Fig. S21 Digital photograph of the S@Cu foam cathode after 6th cycles in full cell Mg-metal battery configuration.

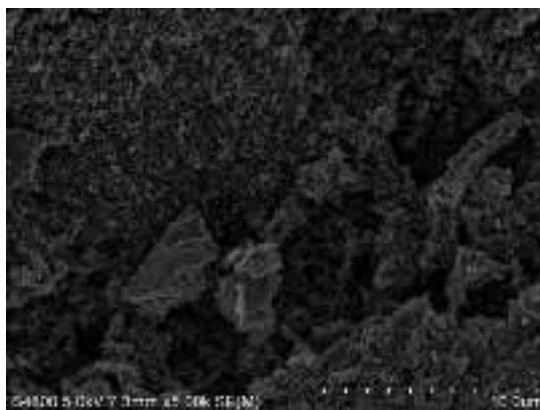


Fig. S22 SEM image of the S@Cu foam cathode after 6th cycles.

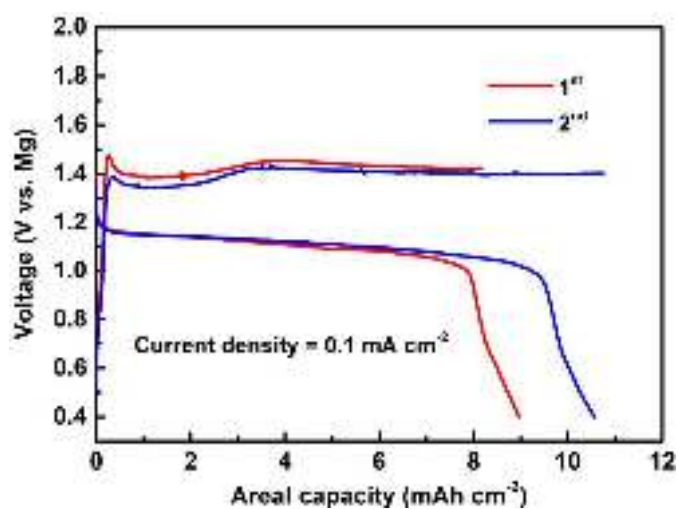


Fig. S23 Galvanostatic charge-discharge profile of the reassembled cell using the S@Cu foam cathode after 6th cycles coupled with fresh Mg anode.

Table S1 Comparison of electrochemical properties of the previously reported Mg-metal batteries.

Cathodes	Electrolyte	Active material loading	Areal capacity
Mo ₆ S ₈ ¹	PhMgCl + AlCl ₃	~1 mg/cm ²	~0.1 mAh/cm ²
Ti ₂ S ₄ ²	PhMgCl + AlCl ₃	N/A	N/A (195 mAh/g)
TiS ₂ ³	PhMgCl + AlCl ₃ +PY14Cl	~1 mg/cm ²	0.4 mAh/cm ²
MoS ₂ ⁴	Mg[B(HFP) ₄] ₂	1.5 mg/cm ²	0.18 mAh/cm ²
VS ₄ ⁵	PhMgCl + AlCl ₃	2 mg/cm ²	0.35 mAh/cm ²
VOPO ₄ ⁶	PhMgCl + AlCl ₃	1.8 mg/cm ²	0.56 mAh/cm ²
CuS ⁷	PhMgCl + AlCl ₃	7 mg/cm ²	0.84 mAh/cm ²

TiO _{2-x} ⁸	PhMgCl + AlCl ₃	2 mg/cm ²	0.3 mAh/cm ²
S-nitrogen doped graphene ⁹	[Mg(THF) ₆][AlCl ₄] ₂	N/A	N/A (700 mAh/g)
S-active carbon cloth ¹⁰	Mg(TFSI) ₂	1 mg/cm ²	1.2 mAh/cm ²
S-carbon ¹¹	Mg(TFSI) ₂ +MgCl ₂	0.75 mg/cm ²	0.99 mAh/cm ²
S-carbon black ¹²	HMDSMgCl + AlCl ₃	N/A	N/A (1200 mAh/g)
S-activated carbon cloth ¹³	(HMDS) ₂ Mg + AlCl ₃ +LiTFSI	0.5 mg/cm ²	0.5 mAh/cm ²
S-CMK400PEG ¹⁴	(HMDS) ₂ Mg + AlCl ₃	N/A	N/A (800 mAh/g)
S-carbon nanofiber ¹⁵	(HMDS) ₂ Mg + AlCl ₃	~1 mg/cm ²	~1.2 mAh/cm ²
S-amorphous mesoporous carbon ¹⁶	BCM	1.5 mg/cm ²	1.62 mAh/cm ²
S-CMK3 ^{17, 18}	Mg[B(HFP) ₄] ₂	1 mg/cm ²	0.93 mAh/cm ²
S-CNT ¹⁹	[Mg ₄ Cl ₆ (DME) ₆][B(HFP) ₄] ₂	1.5 mg/cm ²	1.87 mAh/cm ²
This work/S@Cu foam cathode	[Mg ₄ Cl ₆ (DME) ₆][B(HFP) ₄] ₂	33.3 mg/cm ²	34.2 mAh/cm ²

References

1. Y. Cheng, L. R. Parent, Y. Shao, C. Wang, V. L. Sprenkle, G. Li and J. Liu, *Chemistry of Materials*, 2014, **26**, 4904-4907.
2. X. Sun, P. Bonnick, V. Duffort, M. Liu, Z. Rong, K. A. Persson, G. Ceder and L. F. Nazar, *Energy & Environmental Science*, 2016, **9**, 2273-2277.
3. H. D. Yoo, Y. Liang, H. Dong, J. Lin, H. Wang, Y. Liu, L. Ma, T. Wu, Y. Li, Q. Ru, Y. Jing, Q. An, W. Zhou, J. Guo, J. Lu, S. T. Pantelides, X. Qian and Y. Yao, *Nature Communications*, 2017, **8**, 339.
4. Z. Li, X. Mu, Z. Zhao-Karger, T. Diemant, R. J. Behm, C. Kübel and M. Fichtner, *Nature Communications*, 2018, **9**, 5115.
5. Y. Wang, Z. Liu, C. Wang, X. Yi, R. Chen, L. Ma, Y. Hu, G. Zhu, T. Chen, Z. Tie, J. Ma, J. Liu and Z. Jin, *Advanced Materials*, 2018, **30**, 1802563.
6. L. Zhou, Q. Liu, Z. Zhang, K. Zhang, F. Xiong, S. Tan, Q. An, Y. M. Kang, Z. Zhou and L. Mai, *Adv Mater*, 2018, **30**, e1801984.
7. F. Y. Xiong, Y. Q. Fan, S. S. Tan, L. M. Zhou, Y. A. Xu, C. Y. Pei, Q. Y. An and L. Q. Mai, *Nano Energy*, 2018, **47**, 210-216.
8. Y. Wang, X. Xue, P. Liu, C. Wang, X. Yi, Y. Hu, L. Ma, G. Zhu, R. Chen, T. Chen, J. Ma, J. Liu and Z. Jin, *ACS Nano*, 2018, **12**, 12492-12502.
9. W. Li, S. Cheng, J. Wang, Y. Qiu, Z. Zheng, H. Lin, S. Nanda, Q. Ma, Y. Xu, F. Ye, M. Liu, L. Zhou and Y. Zhang, *Angewandte Chemie*, 2016, **128**, 6516-6520.
10. T. Gao, X. Ji, S. Hou, X. Fan, X. Li, C. Yang, F. Han, F. Wang, J. Jiang and K. Xu, *Advanced Materials*, 2017.
11. A. Robba, A. Vizintin, J. Bitenc, G. Mali, I. Arçon, M. Kavčič, M. Žitnik, K. Bučar, G. Aquilanti, C. Martineau-Corcós, A. Randon-Vitanova and R. Dominko, *Chemistry of Materials*, 2017, DOI: 10.1021/acs.chemmater.7b03956.
12. H. S. Kim, T. S. Arthur, G. D. Allred, J. Zajicek, J. G. Newman, A. E. Rodnyansky, A. G. Oliver, W. C. Boggess and J. Muldoon, *Nat Commun*, 2011, **2**, 427.
13. T. Gao, M. Noked, A. J. Pearse, E. Gillette, X. Fan, Y. Zhu, C. Luo, L. Suo, M. A. Schroeder and K. Xu, *Journal of the American Chemical Society*, 2015, **137**, 12388-12393.
14. Z. Zhao-Karger, X. Zhao, D. Wang, T. Diemant, R. J. Behm and M. Fichtner, *Advanced Energy Materials*, 2015, **5**, n/a-n/a.
15. X. Yu and A. Manthiram, *ACS Energy Letters*, 2016, **1**, 431-437.
16. Z. Zhang, Z. Cui, L. Qiao, J. Guan, H. Xu, X. Wang, P. Hu, H. Du, S. Li and X. Zhou, *Advanced Energy Materials*, 2017.
17. Z. Zhao-Karger, M. E. G. Bardaji, O. Fuhr and M. Fichtner, *Journal of Materials Chemistry A*, 2017, **5**, 10815-10820.
18. Z. Zhao-Karger, R. Liu, W. Dai, Z. Li, T. Diemant, B. Vinayan, C. Bonatto Minella, X. Yu, A. Manthiram and R. J. Behm, *ACS Energy Letters*, 2018.
19. A. Du, Z. Zhang, H. Qu, Z. Cui, L. Qiao, L. Wang, J. Chai, T. Lu, S. Dong, T. Dong, H. Xu, X. Zhou and G. Cui, *Energy & Environmental Science*, 2017, **10**, 2616-2625.